

Corrosion behaviour of porous Ti intended for biomedical applications

A. C. Alves¹ · I. Sendão¹ · E. Ariza^{1,2} · F. Toptan^{1,3} · P. Ponthiaux⁴ · A. M. P. Pinto^{1,3}

© Springer Science+Business Media New York 2016

Abstract Porous Ti implants are being developed in order to reduce the biomechanical mismatch between the implant and the bone, as well as increasing the osseointegration by improving the bone in-growth. Most of the focus in the literature has been on the structural, biological and mechanical characterization of porous Ti whereas there is limited information on the electrochemical characterization. Therefore, the present work aims to study the corrosion behaviour of porous Ti having 30 and 50 % of nominal porosity, produced by powder metallurgy route using the space holder technique. The percentage, size and distribution of the pores were determined by image analysis. Electrochemical tests consisting of potentiodynamic polarization and electrochemical impedance spectroscopy were performed in 9 g/L NaCl solution at body temperature. Electrochemical studies revealed that samples presented a less stable oxide film at increased porosity, more specifically, the complex geometry and the interconnectivity of the pores resulted in formation of less protective oxide film in the pores.

Keywords Powder metallurgy · Space holder · Porous Ti · Corrosion

1 Introduction

Titanium and its alloys are widely used in biomedical implants due to their high corrosion resistance, adequate biocompatibility, and mechanical properties. However, the biomechanical mismatch of Young's modulus between bone and titanium implants (10–30 and 110 GPa, respectively), interfacial instability with the host tissues and lack of biological anchorage are problems yet to be solved [1–4].

Porous Ti implants having open-cellular structure are being developed not just to reduce the biomechanical mismatch, but as well due to the possibility of the new-bone tissue in-growth and the transport of the body fluids [2, 3, 5], or even for their potential use on drug delivery systems [6].

Ti foams have been developed by various processing methods such as selective laser melting, loose powder sintering, slurry foaming, hollow sphere sintering, and powder metallurgy with space-holder techniques [2, 3, 6–8]. Among these methods, most of the efforts have been focused on powder metallurgy with space-holder technique for the last decade because it can be used for manufacturing porous structures easily by avoiding harmful reactions and high processing cost [2, 9–12]. Powder metallurgy route using the space holder technique allows a high degree of freedom in tailoring the foam architecture, namely controllable pore fraction, size, and morphology [2, 13, 14].

It is known that increased porosity is beneficial for bone in-growth, however porosity results in a decrease in mechanical properties. Thus, a balance should be find

✉ A. C. Alves
alexandra@dem.uminho.pt

¹ CMEMS-UMinho - Center of MicroElectroMechanical Systems, Universidade do Minho, Azurém, 4800-058 Guimarães, Portugal

² SEMAT/UM, Universidade do Minho, Azurém, 4800-058 Guimarães, Portugal

³ Dept. Eng. Mecânica, Universidade do Minho, Azurém, 4800-058 Guimarães, Portugal

⁴ Laboratoire de Génie des Procédés et Matériaux-LGPM, École Centrale de Paris, Grande Voie des Vignes, 92290 Châtenay-Malabry, France

between mechanical and biological performance [15, 16]. There are several studies in the literature on microstructural characterization, mechanical properties, and biological response of the porous metallic implants [2, 3, 5, 12, 17–21] but, there is a limited information on their electrochemical behaviour [22, 23].

Studies showed that porosity can alter the corrosion behaviour of materials [22–26]. Seah et al. [25] studied the effects of porosity on corrosion behaviour, particularly, on localised corrosion resistance of sintered porous pure titanium by performing cyclic polarisation tests. The authors reported that lower porosity led to localized corrosion due to the trapping of electrolyte species and the exhaustion of oxygen in the small, isolated pores. However, localized corrosion was not observed on the samples having higher amount of porosity where large and interconnected pores allowed the flow of the electrolyte. Menini et al. [23] compared the corrosion behaviour of dense Ti with highly porous (~73.5–75 %) Ti foams having relatively large (430–650 μm) and interconnected porosity and reported that the foams exhibited slightly higher resistance to corrosion in simulated body fluid (SBF) at body temperature. As opposed to Seah et al. [25], the authors used electrochemical impedance spectroscopy (EIS) and reported that the difference on the corrosion behaviour was associated with the nature and the structure of the oxide film formed on the sample surfaces.

In order to have a better understanding of the effect of porosity on the corrosion behaviour of Ti, comparative studies are needed to be performed with a particular focus on the nature of the passive film formed on the open and closed pore surfaces. Thus, the aim of this study was to investigate the corrosion behaviour of porous Ti having moderate levels of porosity containing isolated and interconnected pores.

2 Materials and methods

Porous Ti samples were processed by powder metallurgy with space holder technique using angular shaped Ti powders having average size of 36 μm (Grade 2, Alfa Aesar), together with angular shaped urea particles under 500 μm (Scharlau) as space holder, and PVA as binder (Sigma Aldrich Chemistry).

Differential thermal analysis and thermal gravimetric analysis (DTA/TG) were performed on powder blends with a heating rate of 5 $^{\circ}\text{C}/\text{min}$ in high purity Ar atmosphere till 600 $^{\circ}\text{C}$ in order to define the binder and space holder removal temperature (SDT 2960 Simultaneous DSC-TGA). In order to determine the sintering temperature, dilatometric analysis was performed under the identical

conditions that were used for the DTA/TG analysis (Linseis, mod.4 L70-2000).

Titanium, urea (30 and 50 vol%) and PVA (0.4 vol%) powder mixtures were prepared by using a ball mill rotating with alumina balls at 130 rpm during 4 h. After mixing, the powder blends were uniaxially pressed in a zinc stearate lubricated nitrided stainless steel die under 350 MPa for 2 min. Cylindrical green compacts 12 mm in diameter and 5 mm in height were pre-heated in argon atmosphere at 500 $^{\circ}\text{C}$ during 3 h for binder and space holder removal, and sintered in horizontal tubular furnace under high vacuum ($<10^{-5}$ mbar) at 1100 $^{\circ}\text{C}$ during 3 h where heating and cooling rates were kept constant as 5 $^{\circ}\text{C}/\text{min}$.

Electrochemical tests consisting of potentiodynamic polarization and electrochemical impedance spectroscopy (EIS) were performed in 9 g/L NaCl at body temperature (37 ± 2 $^{\circ}\text{C}$) using Gamry Potentiostat/Galvanostat (model Reference—600).

A conventional three-electrode electrochemical cell (adapted from ASTM: G3-89) with an electrolyte volume of 180 ml was used, where a saturated calomel electrode (SCE) was used as the reference electrode, a Pt electrode was used as the counter electrode, and the samples having a geometric exposed area of 0.6 cm^2 were used as the working electrode. For the porous samples, the exposed area (A_e) was calculated with the following formula assuming that the pores have spherical shapes:

$$A_e = A_g + \left(\frac{1}{2} \sum_{i=1}^n 4\pi r_{i\text{por}}^2 \right) - \left(\sum_{i=1}^n \pi r_{i\text{por}}^2 \right) \quad (1)$$

where A_g is the geometric area and r_{por} is the pore radius that is obtained by image analysis. According to Eq. (1), the exposed areas were calculated as 0.67 ± 0.01 and 0.71 ± 0.02 cm^2 for Ti22 and Ti37 groups, respectively.

The impedance data acquisition was performed after stabilization at open circuit potential (OCP). The OCP was considered stable when ΔE was below 60 mV h^{-1} . EIS measured by scanning a range of frequencies from 63 kHz till 10 mHz, with 10 points per frequency decade, and the amplitude of the sinusoidal signal was 10 mV in order to guarantee the linearity of the electrode response. Potentiodynamic polarization tests were performed with a scanning rate of 1 mV/s in the anodic direction from -0.6 V till 1.5 V versus SCE.

Microstructures were examined by using a Leica DM2500 optical microscope (OM) and a FEI Nova 200 field emission gun scanning electron microscope (FEG-SEM), equipped with EDAX-Pegasus energy dispersive X-ray spectroscopy (EDS). The size distribution and fraction of pores were determined by image analysis technique

using Leica DM2500 OM and Image J 1.37v image analysis software.

3 Results and discussion

DTA/TG curves obtained from Ti–urea (50 vol%) – PVA (0.4 vol%) powder mixture are given in Fig. 1. Five endothermic peaks were observed on the DTA curve at around the values of 140, 190, 210, 250, and 350 °C. The endothermic reactions were dominated by different chemical processes associated with the mass loss stages observed in the TG curve. It is known from the literature that urea melts, decomposes, and evaporates within a short temperature range. The first endothermic peak and the beginning of the major mass loss step around 140 °C is related with melting of urea. The region between 140 and 210 °C is characterized by the mass loss due to the decomposition of urea into biuret. From 210 till 250 °C, urea decomposition continues and biuret begins to decompose. Finally, the last peak observed around 350 °C is related with the continued sublimation, decomposition and elimination of the remaining products [27–30]. On the other hand, the TG curve revealed weight loss till approximately 450 °C. Thus, due to the DTA/TG analysis, the space-holder and binder removal temperature was chosen as 450 °C.

Figure 2 presents the shrinkage rate as a function of temperature for titanium. No significant dimensional variations were observed till around 800 °C, whereas maximum shrinkage rates were observed between 1080 and 1220 °C. Similar results have also been reported by Bolzoni et al. [31] where no significant dimensional variation was observed till 870 °C for CP Ti. The authors stated that the beginning of the shrinkage process corresponds to the allotropic phase transformation of Ti from HCP (α) to BCC

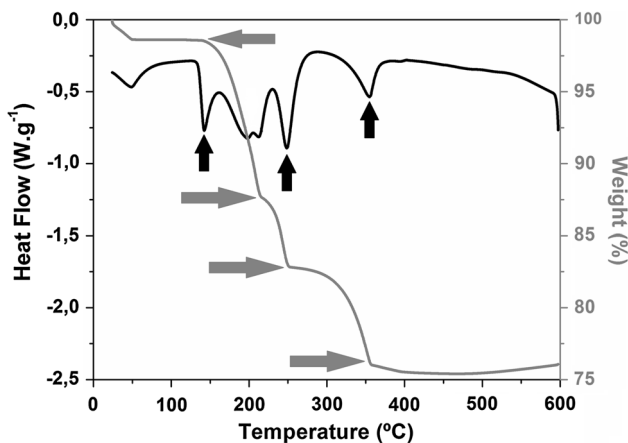


Fig. 1 DTA-TG curves of titanium–urea–PVA powder blend

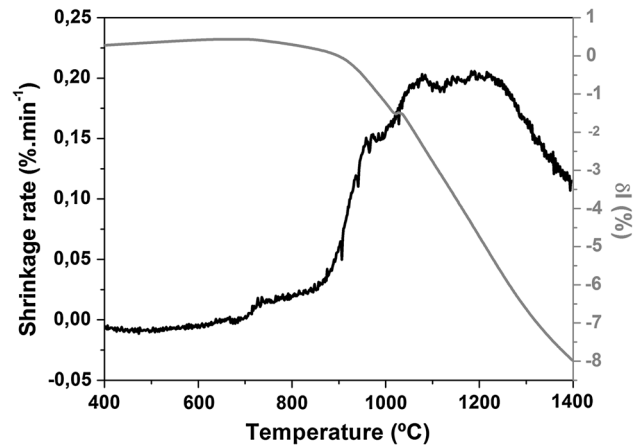


Fig. 2 Shrinkage rate as a function of temperature for titanium powders

(β) phase. It was also reported that the total amount of residual porosity was significantly lower at 1100 °C. Above this temperature, the residual porosity continued to be decreased, however, pronounced grain growth was reported. Therefore, according to the dilatometric analysis and the reported results in the literature, the sintering temperature was chosen as 1100 °C.

Table 1 presents the measured porosity values obtained by image analysis technique. As can be seen on the results, measured porosity values were lower than the nominal porosity (i.e. volume fraction of the urea in the powder mixture). Reduction of the porosity after sintering can be attributed to the shrinkage that has previously been reported as increased with the increasing space holder content [32, 33]. Laptev et al. [32] stated that when space holder is used, the Ti framework is less densified due to the bridges of the space holder particles deteriorating the pressure transfer to the Ti particles. Accordingly, the density of the Ti framework decreases with the increased amount of space holder resulting in higher shrinkage during sintering [32].

Quantitative results for pore size on Ti22 and Ti37 groups are given in Fig. 3. About 80 % of the pores in both groups were in the range of 50–350 μm . The average pore size was 230 and 200 μm for Ti22 and Ti37 groups, respectively.

The morphology and distribution of the pores can be seen on the OM images given in Fig. 4. Residual porosity

Table 1 Porosity values for each group of samples

Samples	Porosity (%)
Dense Ti (Ti)	0.4 \pm 0.1
Ti-30 % vol. urea (Ti22)	22 \pm 2
Ti-50 % vol. urea (Ti37)	37 \pm 2

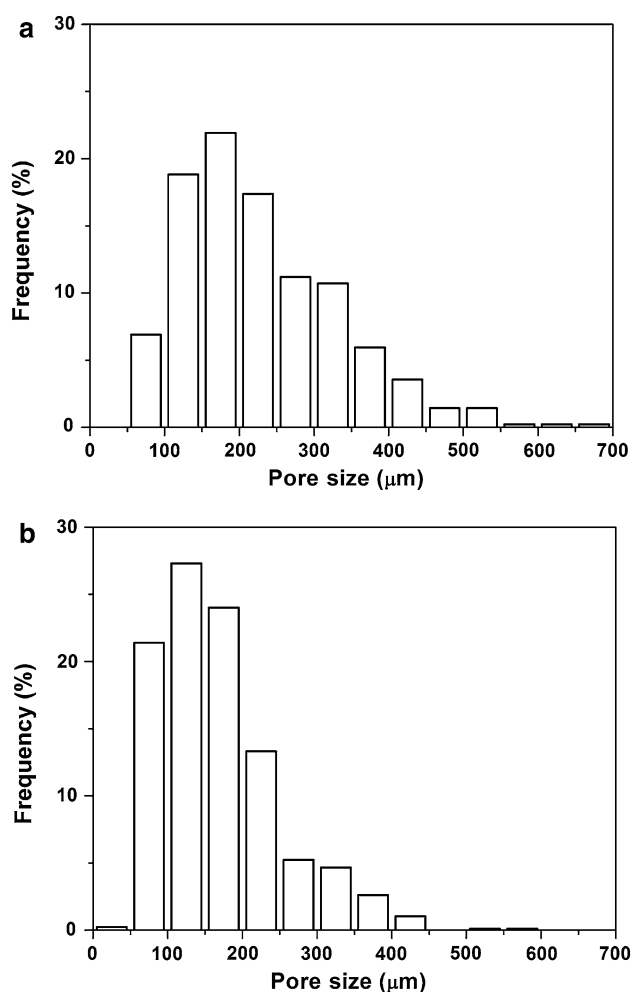


Fig. 3 Pore size distribution on **a** Ti22 and **b** Ti37 groups

can be seen on the dense Ti samples as a natural consequence of powder sintering [34] (Fig. 4a). When the amount of space holder increased from 30 to 50 % (vol.), interconnected pores were formed in addition to the isolated pores (Fig. 4b, c).

Figure 5 shows the representative potentiodynamic polarization curves for the dense and porous samples in 9 g/L NaCl at body temperature. As can be seen on the

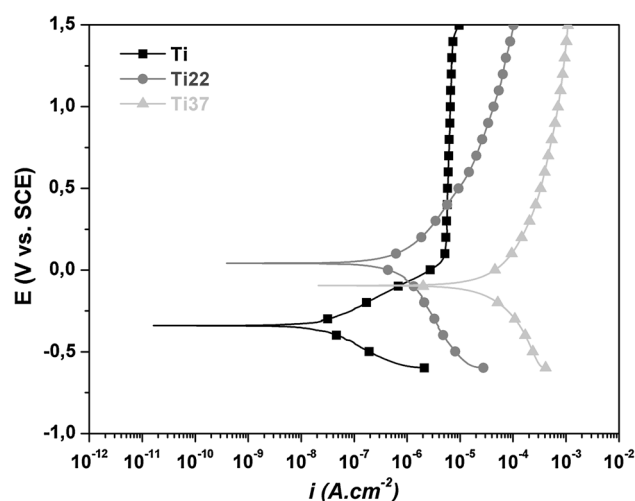


Fig. 5 Potentiodynamic polarization curves

results, Ti samples exhibited a lower corrosion potential, together with a well-defined passivation plateau obtained above 200 mV. Ti22 and Ti37 samples presented $E_{(i=0)}$ slightly higher than Ti samples. Although no passivation plateau was observed, porous samples exhibited a passivation region. The lack of a well-defined passivation plateau can be attributed to the heterogeneities of the oxide film formed on the most inner pores. Additionally, due to the difficulty on the electrolyte penetration through the pores as well as the difficulty on the oxygen diffusion might lead to a difference on the thickness and the nature of the oxide layers between Ti22 and Ti37. As well, the formation rate of the oxide layer might be different on the inner pores. Moreover, porous samples exhibited higher i_{corr} values as compared to the dense samples being in accordance with the literature [35–37].

Seah et al. [25] studied the influence of pore morphology on corrosion behaviour of Ti. The authors suggested that isolated pores may promote the trapping of electrolyte species leading to lack of oxygen supply that is crucial to the maintenance of a stable titanium oxide film. On the other hand, open and interconnected pore morphology

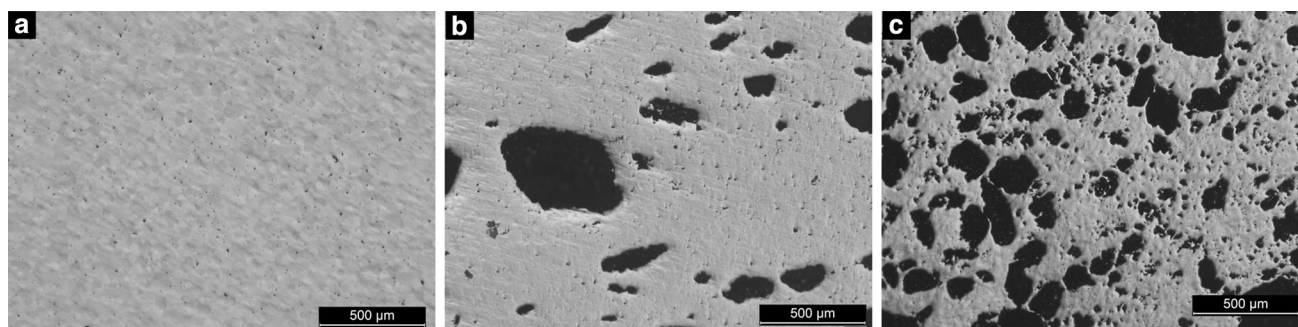


Fig. 4 OM images of **a** Ti, **b** Ti22, and **c** Ti37 samples

will allow the electrolyte species to flow freely and replace the oxygen supply during the passivation.

Fojt et al. [37] studied the corrosion behaviour of porous Ti39Nb alloy processed by powder metallurgy and reported that samples till 15 % of porosity exhibited similar corrosion behaviour to the dense samples, however, localized corrosion has been observed above this porosity value. Xie et al. [35] studied the corrosion behaviour of porous TiMo alloy obtained by laser sintering and reported that after the Tafel region, samples having 24–32 % porosity transposed directly into the passive region whereas the samples having 55–65 % porosity exhibited several active–passive transitions before passive region. The authors attributed this difference on the passive film formed on the highly porous samples that was reported as not protective enough when immersed into the electrolyte.

Figure 6 presents the representative electrochemical impedance spectra in form of Nyquist and Bode diagrams. It can be observed from Nyquist diagram that the dense samples presented a larger diameter of semi-circle suggesting a higher corrosion resistance as compared to the porous samples. Regarding the porous samples, the semi-circle diameter was smaller for Ti37 as compared to Ti22. In high frequency range (10^2 – 10^5 Hz), constant values of $|Z|$ was observed in Bode diagram for the dense samples where the phase angle was near 0° as the response of the electrolyte resistance. In low and middle frequency ranges, the phase angle presented values approached 90° which is a typical capacitive behaviour of a compact oxide film. On the other hand, Bode diagram exhibited two time constants for the porous samples representing the most external pores

on the middle frequencies and the inner pores on the low frequencies where the complex geometry of the inner pores may slow down the penetration of the electrolyte. Besides, the values of the phase angle for each time constant were always lower for Ti37 as compared to Ti22. It can be stated by comparing $|Z|$ values in low frequencies that dense samples presented the highest values indicating a higher impedance modulus of the system leading to a better corrosion behaviour.

Figure 7 gives the schematic presentation of the equivalent circuits used for fitting the EIS results, together with representative SEM images. The equivalent circuit of the native oxide film formed on the surface of Ti samples (Fig. 7a) contains electrolyte resistance, R_e , native oxide film resistance, R_{ox} , and constant phase element (CPE), Q_{ox} , considering a non-ideal capacitance of the native oxide film. Figure 7b represents the equivalent circuit for the Ti22 samples having an oxide film both on the outmost surface and on the pore surfaces. Since these oxides films have different nature and quality, they have their own resistance and capacitance. It was assumed that the surface oxide film is more protective than the oxide film formed inside of the pores, therefore its resistance may be considered as too high to be included in the model. Therefore, the resistance element corresponding to Q_{ox} was not included in the circuit due to its insulating behaviour. An additional electrolyte resistance ($R_{e'}$) was added to the circuit as contribution of the electrolyte inside of the pores. Once that the oxide film inside of the pore is less protective, its resistance (R_{op}) should be considered in the model. Therefore, the pair (R_{op}/Q_{op}) was obtained.

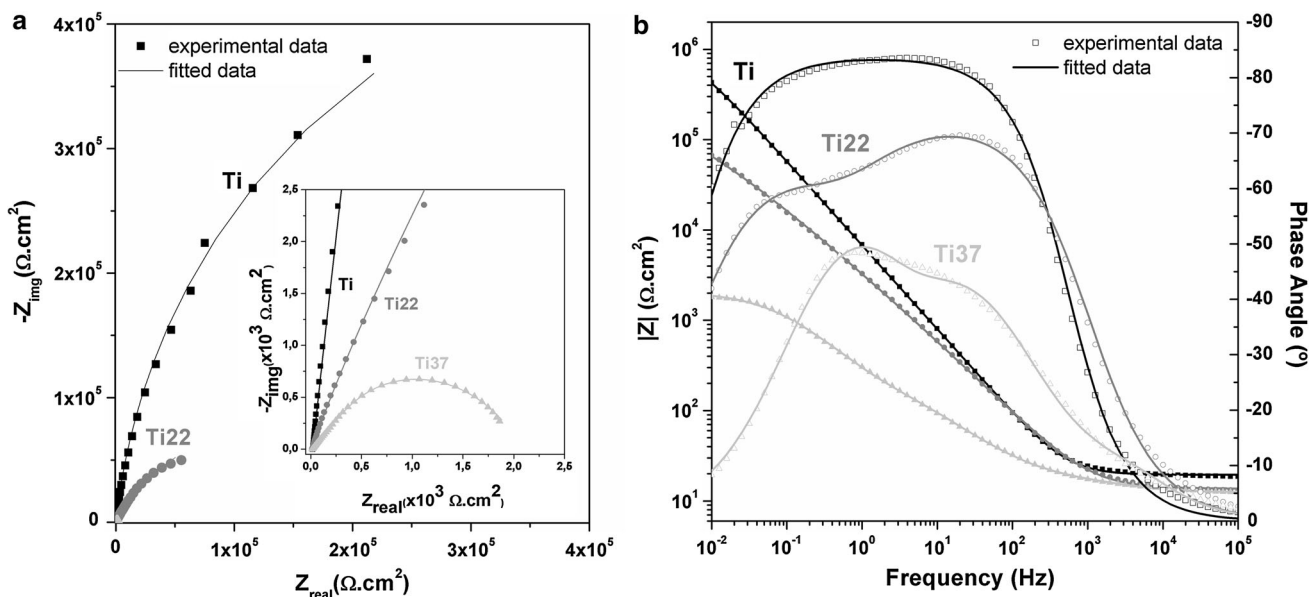


Fig. 6 EIS spectra in the form a Nyquist and b Bode diagrams

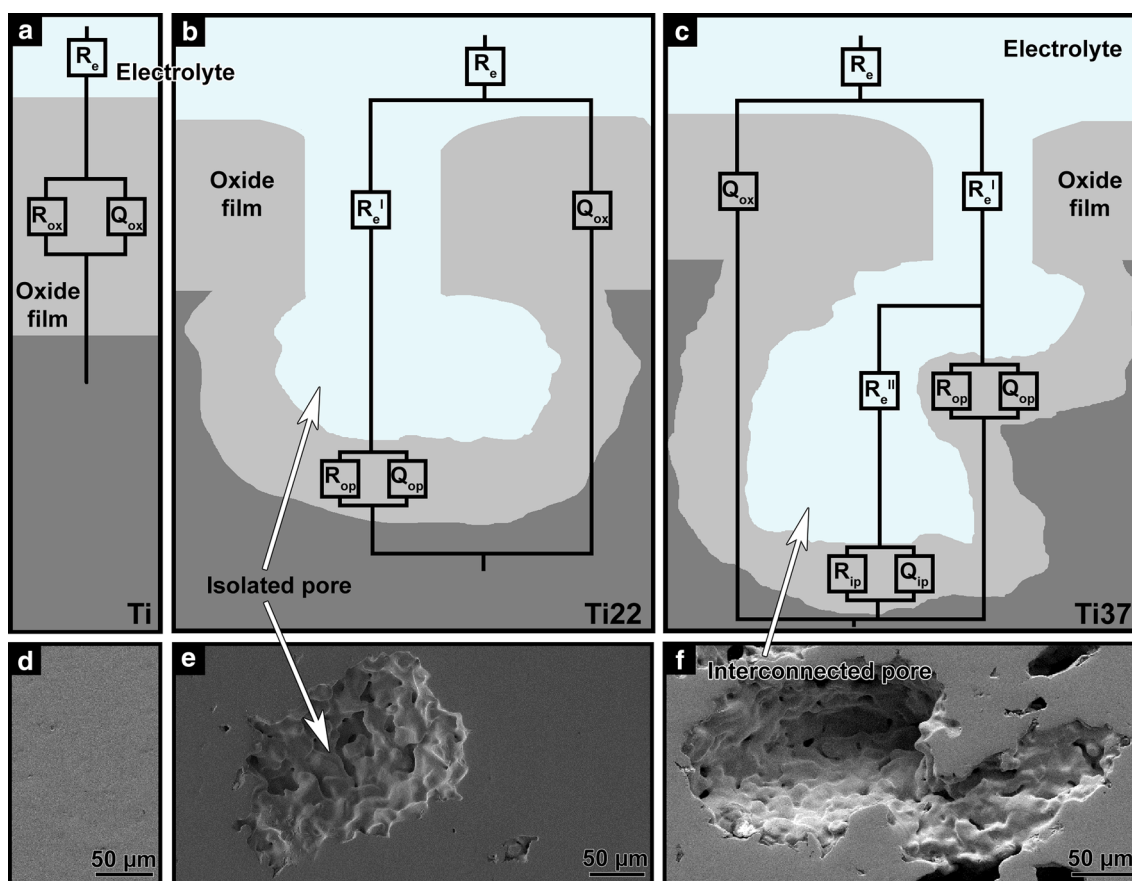


Fig. 7 Equivalent circuits (a–c) and representative secondary electron SEM images (d–f) of Ti, Ti22 and Ti37 samples, respectively

Xie et al. [35] used a similar equivalent circuit showed in Fig. 7b to fit the experimental data on TiMo alloy having 24 and 32 % of porosity. The authors concluded that by increasing the porosity, the resistance of the superficial oxide film decreased while capacitance increased. Regarding the oxide layer formed at the inner pore space, the authors reported a drastic decrease on the resistance values and a significant increase on the capacitance values. The equivalent circuit used for Ti37 samples (Fig. 7c) contains the same pairs described for Ti22 but a third pair (R_{ip}/Q_{ip}) was also added in order to describe in the lower frequencies range, the most internal pores and its interconnectivity. Moreover, an additional electrolyte resistance ($R_{e''}$) was also included to the circuit as contribution of the electrolyte inside of the most internal pores.

Instead of a capacitor, a CPE was used in the fitting allowing the representation of a non-ideal capacitor. The impedance of CPE is defined as:

$$Z_{CPE} = [Y_0(j\omega)^n]^{-1} \quad (2)$$

where $-1 \leq n \leq 1$. When $n = 1$, $n = 0$, and $n = -1$, the CPE response corresponds to those of a capacitor, a resistor or an inductor, respectively. When $n \cong 1$, a non ideal

capacitor may be described by this element, n value is influenced by the roughness of the surface and its heterogeneity [38]. All groups of samples presented n values higher than 0.75.

The impedance spectra for all groups of samples were fitted to the corresponded equivalent circuit using Gamry Echem Analyst (version 5.61) and the quality of the fitting was evaluated through their goodness of fitting values. In all cases the goodness of fitting values were below 10^{-3} .

The equivalent circuit parameters obtained from EIS data are presented in Table 2. The values of the compact oxide layer capacitance were lower on the dense samples as compared to the porous ones. It is known that low values of capacitance indicates a good quality of the passive film [35]. Dense and porous Ti samples presented similar Q_{ox} values indicating that the oxide film formed on the surface had similar protective properties. The values of the total impedance of the system were around 10^6 , 10^5 , and $10^4 \Omega \text{ cm}^2$ for Ti, Ti22, and Ti37, respectively. It is known that the total system resistance values higher than $10^6 \Omega \text{ cm}^2$ indicates the formation of an oxide film on passive state. Moreover, R_p below $10^6 \Omega \text{ cm}^2$ indicates that the surface is still on the active state, pointing an

Table 2 Equivalent circuit parameters obtained from EIS data

	R_{ox} (Ω cm ²)	Q_{ox} (μ F cm ⁻²)	R_{op} (Ω cm ²)	Q_{op} (μ F cm ⁻²)	R_{ip} (Ω cm ²)	Q_{ip} (μ F cm ⁻²)
Ti	$(1.02 \pm 0.26) \times 10^6$	31 ± 9	–	–	–	–
Ti22	–	34 ± 4	$(1.6 \pm 0.4) \times 10^5$	97 ± 36	–	–
Ti37	–	36 ± 7	$(3.0 \pm 0.8) \times 10^3$	592 ± 47	$(2.8 \pm 0.3) \times 10^3$	531 ± 221

unstable oxide film [39]. Therefore, these results suggested that the increase on the porosity led to less protective oxide film. This phenomenon may be associated to the difficulty of the electrolyte to penetrate and fill the pores, leading to a slower the growth of the protective passive film which may also lead to formation of heterogeneous film mainly of its thickness.

Ti22 presented slightly lower Q_{op} values as compared to Ti37 that may be related to the nature of the pores. Bigger but close pores on Ti22 may facilitate the penetration and filling of the electrolyte into the pores leading to a formation of a slightly more stable and more protective oxide film as compared to the Ti37 samples.

4 Conclusions

Porous Ti having closed and interconnected pores were produced by powder metallurgy route using the space holder technique and their corrosion behaviour were investigated in 9 g/L NaCl solution at body temperature. Potentiodynamic polarization tests showed that porous samples did not present a passivation plateau and exhibited higher corrosion current values. EIS studies revealed that porous samples presented a less stable oxide film leading to lower protection properties. At higher porosity, the complex geometry and the interconnectivity of the pores resulted in less protective oxide film formed in the pores due to the difficulties on the penetration of the electrolyte thorough the inner pores.

In order to validate the presented models, further studies with different levels of porosity are needed to be performed.

Acknowledgments This study was supported by FCT with the reference project UID/EEA/04436/2013, by FEDER funds through the COMPETE 2020 – Programa Operacional Competitividade e Internacionalização (POCI) with the reference project POCI-01-0145-FEDER-006941, Programa de Acções Universitárias Integradas Luso-Francesas’ (PAULF TC-12_14), and The Calouste Gulbenkian Foundation through “Programa de Mobilidade Académica para Professores”. The authors would also like to acknowledge Prof. Ana Senos (University of Aveiro) and Prof. José Carlos Teixeira (University of Minho) for the provision of the characterization facilities.

References

- C.A.H. Laurindo, R.D. Torres, S.A. Mali, J.L. Gilbert, P. Soares, *Mater. Sci. Eng. C* **37**, 223 (2014)
- B. Lee, T. Lee, Y. Lee, D.J. Lee, J. Jeong, J. Yuh, S.H. Oh, H.S. Kim, C.S. Lee, *Mater. Des.* **57**, 712 (2014)
- S. Amin Yavari, S.M. Ahmadi, J. van der Stok, R. Wauthle, A.C. Riemslog, M. Janssen, J. Schrooten, H. Weinans, A.A. Zadpoor, *J. Mech. Behav. Biomed. Mater.* **36**, 109 (2014)
- F.A. España, V.K. Balla, S. Bose, A. Bandyopadhyay, *Mater. Sci. Eng. C* **30**, 50 (2010)
- V. Goriainov, R. Cook, J.M. Latham, D.G. Dunlop, R.O.C. Oreffo, *Acta Biomater.* **10**, 4043 (2014)
- N. Jha, D.P. Mondal, J. Dutta Majumdar, A. Badkul, A.K. Jha, A.K. Khare, *Mater. Des.* **47**, 810 (2013)
- D.C. Dunand, *Adv. Eng. Mater.* **6**, 369 (2004)
- B. Vamsi Krishna, W. Xue, S. Bose, A. Bandyopadhyay, *JOM* **60**, 45 (2008)
- J.A. Lyndon, B.J. Boyd, N. Birbilis, *J. Control. Release* **179**, 63 (2014)
- M.E. Dizlek, M. Guden, U. Turkan, A. Tasdemirci, *J. Mater. Sci.* **44**, 1512 (2008)
- X. Fan, B. Feng, J. Weng, J. Wang, X. Lu, *Mater. Lett.* **65**, 2899 (2011)
- B. Dabrowski, W. Swieszkowski, D. Godlinski, K.J. Kurzydowski, *J. Biomed. Mater. Res. B Appl. Biomater.* **95**, 53 (2010)
- W. Niu, C. Bai, G. Qiu, Q. Wang, *Mater. Sci. Eng. A* **506**, 148 (2009)
- J. Jakubowicz, G. Adamek, M. Dewidar, *J. Porous Mater.* **20**, 1137 (2013)
- L. Chen, T. Li, Y. Li, H. He, Y. Hu, *Trans. Nonferrous Met. Soc. China* **19**, 1174 (2009)
- Y. Bao, M. Zhang, Y. Liu, J. Yao, Z. Xiu, M. Xie, X. Sun, *J. Porous Mater.* **21**, 913 (2014)
- S. Kashef, A. Asgari, T.B. Hilditch, W. Yan, V.K. Goel, P.D. Hodgson, *Mater. Sci. Eng. A* **527**, 7689 (2010)
- M.H. Lee, K.B. Kim, J.H. Han, J. Eckert, D.J. Sordelet, *J. Phys. D Appl. Phys.* **41**, 105404 (2008)
- X. Li, C. Wang, W. Zhang, Y. Li, *Mater. Lett.* **63**, 403 (2009)
- J.P. Li, S.H. Li, C.A. Van Blitterswijk, K. de Groot, *J. Biomed. Mater. Res. A* **73**, 223 (2005)
- K. Kato, S. Ochiai, A. Yamamoto, Y. Daigo, K. Honma, S. Matano, K. Omori, *Acta Biomater.* **9**, 5802 (2013)
- F.X. Xie, X.B. He, S.L. Cao, X. Lu, X.H. Qu, *Corros. Sci.* **67**, 217 (2013)
- R. Menini, M.-J. Dion, S.K.V. So, M. Gauthier, L.-P. Lefebvre, *J. Electrochem. Soc.* **153**, B13 (2006)
- K.H.W. Seah, X. Chen, *Corros. Sci.* **34**, 1841 (1993)
- K.H.W. Seah, R. Thampuran, S.H. Teoh, *Corros. Sci.* **40**, 547 (1998)
- Y. Li, G. Rao, L. Rong, Y. Li, *Mater. Lett.* **57**, 448 (2002)
- J.M. Jones, A.N. Rollinson, *Thermochim. Acta* **565**, 39 (2013)
- L. Stradella, M. Argentero, *Thermochim. Acta* **219**, 315 (1993)

29. P.M. Schaber, J. Colson, S. Higgins, D. Thielen, B. Anspach, J. Brauer, *Thermochim. Acta* **424**, 131 (2004)
30. S. Sebelius, T.T. Le, L.J. Pettersson, H. Lind, *Chem. Eng. J.* **231**, 220 (2013)
31. L. Bolzoni, T. Weissgaerber, B. Kieback, E.M. Ruiz-Navas, E. Gordo, *J. Mech. Behav. Biomed. Mater.* **20**, 149 (2013)
32. A. Laptev, M. Bram, H.P. Buchkremer, D. Stöver, *Powder Metall.* **47**, 85 (2004)
33. N. Tuncer, G. Arslan, E. Maire, L. Salvo, *Mater. Sci. Eng. A* **530**, 633 (2011)
34. H.L. Bi, C.Z. Yu, P. Cao, Y.H. He, *Key Eng. Mater.* **520**, 76 (2012)
35. F. Xie, X. He, S. Cao, M. Mei, X. Qu, *Electrochim. Acta* **105**, 121 (2013)
36. G. Xie, F. Qin, S. Zhu, D.V. Louzguine-Lugzin, *Intermetallics* **44**, 55 (2014)
37. J. Fojt, L. Joska, J. Málek, *Corros. Sci.* **71**, 78 (2013)
38. N. Figueira, T.M. Silva, M.J. Carmezim, J.C.S. Fernandes, *Electrochim. Acta* **54**, 921 (2009)
39. D. Mareci, R. Chelariu, D. Gordin, G. Ungureanu, T. Gloriant, *Acta Biomater.* **5**, 3625 (2009)